4th Imeko TC19 Symposium on Environmental Instrumentation and Measurements
Protecting Environment, Climate Changes and Pollution Control
June 3-4, 2013, Lecce, Italy

CONTACTLESS ELEMENTAL AND SIZE ANALYTICAL SYSTEM FOR NANOSIZED SUSPENDED PARTICULATE MATTER USING LIBS AND LII TECHNIQUES

S. Ikezawa and T. Ueda

Graduate School of Information, Production and Systems, Waseda University, 2-7 Hibikino, Wakamatsu, Kitakyushu, Fukuoka, Japan, ikezawa@y.fuji.waseda.jp

Abstract: This paper presents a non-contact sensing system for nanosized suspended particulate matter (SPM) measurements using laser-induced incandescence (LII) and laser-induced breakdown spectroscopy (LIBS). The elemental composition and density of the SPMs are determined using LIBS, and particulate size measurements are accomplished using LII. Typically, temporally resolved LII enables measurement of soot particulate sizes in a combustion process. In the case of the measured object consisting of a single element material, it is easy to determine the particulate sizes distribution derived from the ratio of emission attenuation signals after a laser pulse, because the cooling behaviour is characteristic of the particulate size in LII technique. However, in actuality, the SPMs consist of several different types of elements. The elemental analysis using LIBS also allows correcting the discrepancy between the LII simulation values and observation results.

Keywords: LIBS, LII, SPM, $PM_{2.5}$, nano particulate.

1. INTRODUCTION

Recent regional atmospheric environment issues in large cities of developing countries are related to rapid industrialization and growth of automobile use. Increasing emission of fossil fuel from factories, power plants, and automobiles is recognized as a serious problem. The beta-ray absorption system is the most typical automatic measuring instrument for suspended particulate matter (SPM) in Japan. The main advantages of the beta-ray absorption method are: 1) the mass absorption coefficient is constant with regard to the particulate composition, 2) it does not require as frequent cleaning as does the piezo-balance type dust monitoring method, and 3) unlike the light scattering method, it does not require standard calibration steps that use reference material. However, recently, attention has been focused on designing environmental monitoring systems that can detect particulates smaller than 2.5 μm. It is well known that inhalation of fine particulate matter causes a range of health problems [1–4]. Particulates that are smaller than 2.5 μm in size ($PM_{2.5}$) can penetrate the gas-exchange region of the lungs. This indicates that information on the size of particulates (e.g. distinguishing particulates based on their sizes) is as important as the information on the elemental components and density of particulates. However, it is difficult to simultaneously obtain real-time information on the size and composition of nanosized SPMs. Laser-induced breakdown spectroscopy (LIBS) is a useful tool to determine the elemental composition of various materials, and it does not require any chemical or physical pre-processing steps. However, because of the breakdown of all particulates, the LIBS technique is not sufficient for obtaining information on specific particulate sizes. The quantitative values obtained by LIBS only relate to the total volume of particulates per unit volume; in other words, these values relate to the weight/volume density. A particulate counter, based on the laser light scattering method, has been conventionally employed to measure the size and the distribution of suspended particulates. However, this method requires particulate flow path and proper flow control to guide all particulate into the point of measurement. In this article, we apply the laser-induced incandescence (LII) technique along with the LIBS. The average particulate size is determined by using the simulation on the LII technique. The most striking feature of the combined LIBS and LII system is its ability to perform real-time measurements with non-contact and non-guiding particulates into the measurement spot. The simulation method adopted in this research has undergone one of the most detailed studies available, the one provided by H. A. Michelsen [5]. This calculation approach requires an accurate data or good approximation (Gaussian fit, Voigt fit, etc.) of the laser intensity temporal profile used in the experiment, in order for it to agree with the actual temporal profile of the intensity. The laser intensity profile plays an important role in the theoretical estimation of the energy absorption rate. We demonstrate that an accurate laser intensity profile can be obtained by using a streak camera.

2. EXPERIMENTAL SETUP

Figure 1 shows a schematic of the combined system that consists of LII and LIBS. The optical layout of the system consists of the following devices: a Nd:YAG laser, a spectrograph, a streak camera, and a delay pulse generator.

The Nd:YAG laser was operated at 1064 nm to generate a 50 mJ Q-switched pulse with a width of 8 ns (full width at half maximum, FWHM). The emissions from the particulate target were guided into the spectrograph and dispersed by a grating with a groove density of 1200 lines/mm, photoemissive electrons were temporally resolved using a streak camera, and the data were stored in and processed by a computer. The LII technique is based on the analysis of the cooling behaviour of the particulates after irradiation by the laser pulse. By using the Stefan-Boltzmann law for a black body, the LII signal gives the profile of the intensity decay time depending on the particulate size.

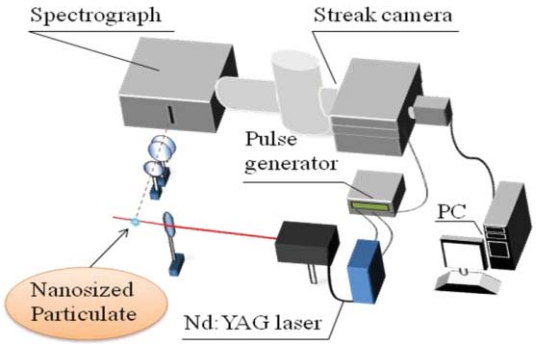

Fig. 1 Schematic of the LII and LIBS combined system

Figure 2 shows the temporal profile of the laser power density for LII measurements.

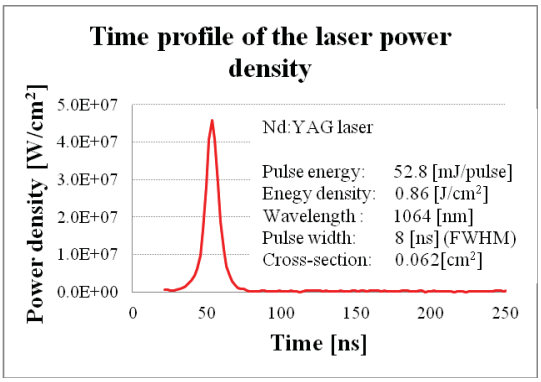

Fig. 2 Temporal profile of laser power density (t = 0 – 250 ns)

3. SIMULATION OF LII

According to the H.A. Michelsen's model, the energy balance for the interaction of a particulate with a laser is given by:

$$Q_{Int} = Q_{abs} - Q_{rad} - Q_{cond} - Q_{sub} + Q_{ann} + Q_{ox}, \qquad (1)$$

where Q_{Int} represents the energy storage in a particulate; Q_{abs} is the rate of laser energy absorption; Q_{rad} is the blackbody emission radiation rate; Q_{cond} represents the rate of energy dissipation by conduction; Q_{sub} represents the rate of energy loss by sublimation of carbon clusters and accounts for energy consumption during photodesorption of the annealed particulate in forming small carbon clusters; Q_{ann} represents the rate of energy production by particulate annealing; and Q_{ox} represents the rate of energy generation by oxidation. Each term in this energy flow rate equation is accounted for by the temporal intensity profile of a laser beam, the time dependence of the particulate temperature, and the initial state of the particulate. The time-derivative term of the particulate temperature dependence yields:

$$\frac{dT}{dt} = \frac{6}{\pi D^3 \rho_S c_S}(Q_{abs} - Q_{rad} - Q_{cond} - Q_{sub} + Q_{ann} + Q_{ox}) \qquad (2)$$

where T is the particulate temperature, D is the primary particulate diameter, ρ_s is the density of the particulate, and c_s is the specific heat of solid carbon. From Planck's equation for a blackbody, the LII signal at wavelength λ' is given by:

$$S = \Omega \pi D^2 \int_\lambda \varepsilon_\lambda \frac{2\pi hc^2}{\lambda'^5 \left[\exp\left(\frac{hc}{\lambda' k_B T}\right) - 1\right]} \Sigma_\lambda(\lambda') d\lambda' \qquad (3)$$

Where Ω is the normalization constant; ε_λ is the emissivity at wavelength λ for a Rayleigh particulate; h is the Planck constant; c is the speed of light; k_B is the Boltzmann constant; and Σ_λ is the integration of the Planck function over wavelength. Solving Eq. (2) gives each term of the energy flow ratio calculated from the laser beam intensity profile that was obtained from the actual measurement.

Absorption: The energy absorption rate was calculated as:

$$Q_{abs} = \frac{\pi^2 D^3 E(m)}{\lambda} q(t) \qquad (4)$$

The intensity profile $q(t)$ is given by the experimental result shown in Fig. 2. The function $E(m)$ is the complex refractive index and can be expressed as:

$$E(m) = \frac{6 n_m k_m}{(n_m^2 - k_m^2 + 2)^2 + 4 n_m^2 k_m^2} \qquad (5)$$

A refractive index of $m = n_m - k_m i$ is given by the laser wavelength (1064 nm) with $n_m = 1.63$ and $k_m = 0.7$. Figure 3 shows the temporal profile of the energy absorption rate caused by the laser, obtained from Eq. (4).

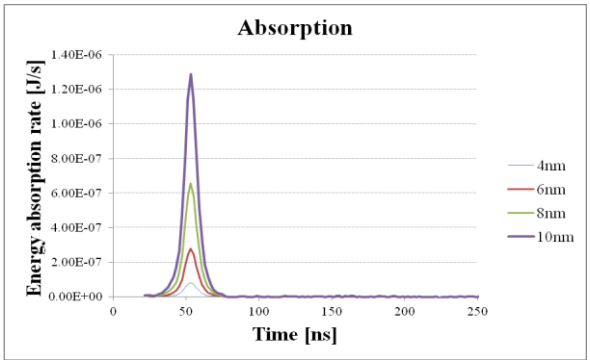

Fig. 3 Variation in the temporal profile of energy absorption rate

Radiation: The rate of radiation was calculated as:

$$Q_{rad} = \frac{199\pi^3 D^3 \left(k_B T\right)^5 E(m)}{h(hc)^3} \qquad (6)$$

Figure 4 shows the temporal profile of the energy loss rate caused by radiation from the particulate. This profile was obtained by successive iterations, starting with the initial temperature of T_0= 1060 K, on the assumption that the measured nano-sized particulates exist in the flame.

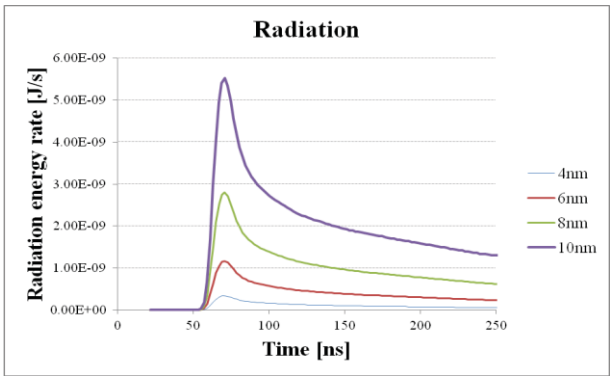

Fig. 4 Variation in the temporal profile of radiation energy rate

Conduction: The thermal conductivity of the soot was calculated as:

$$Q_{cond} = \frac{2\kappa_a \pi D^2}{\left(D + GL\right)}\left(T - T_0\right) \qquad (7)$$

here, κ_a is the thermal conductivity of the surrounding gas (κ_a =1.0811×10^{-4}+5.1519×10^{-7} T_0 was used in this study), L is the mean free path (L = 2.24×10^{-8} T_0 cm/K), and G is the heat transfer factor, given by:

$$G = \frac{8f}{\alpha_T(\gamma + 1)} \qquad (8)$$

where f is the Eucken factor (f = (9γ−5)/4), γ is the heat capacity ratio (γ = 1.3), and α_T is the thermal accommodation coefficient of the ambient combustion gases with the surface (α_T = 0.3). Figure 5 shows the temporal profile of the conduction energy loss rate caused by thermal conductivity of the surrounding gas.

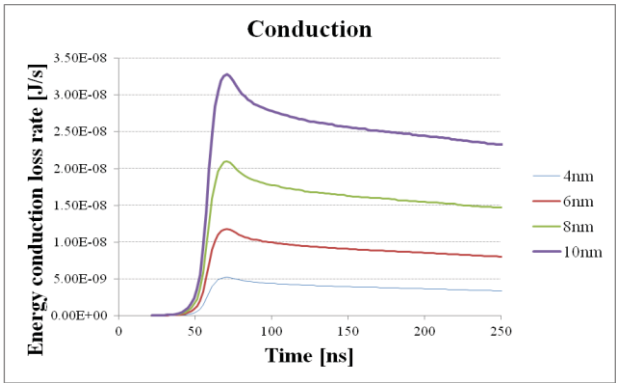

Fig. 5 Variation in the temporal profile of energy conduction loss rate

Sublimation: The sublimation at high temperatures during laser irradiation, producing gas-phase carbon atom clusters, was calculated as:

$$Q_{sub} = \sum_{j=1}^{10} \frac{1}{W_j}\left(\frac{dM}{dt}\right)_j \left[\frac{\Delta H_j\left(P_{sat}{}^{C_j} - P_{phot}{}^{C_j}\right) + \Delta H_{\lambda s} P_{\lambda s} + \Delta H_{diss} P_{diss} + \Delta H_{\lambda a} P_{\lambda a}}{P_{sat}{}^{C_j}}\right] \qquad (9)$$

where the summation is assumed to include contributions from C_1 to C_{10} desorbed species with vaporized molecular weights from W_1 to W_{10}. The quantity ΔH_j is the enthalpy for the formation of the carbon vapour species C_j, $P_{sat}{}^{Cj}$ is the saturation partial pressure of C_j, and $P_{phot}{}^{Cj}$ is the instantaneous partial pressure of C_j from photodesorption of the particulate. The energy required to remove carbon clusters from the unannealed particulate by non-thermal photodesorption is $\Delta H_{\lambda s}$, $P_{\lambda s}$ is the effective pressure calculated from the rate of non-thermal photodesorption from the unannealed particulate, and ΔH_{diss} is the estimated enthalpy of pyrolysis. The effective pressure P_{diss} is calculated from the rate of thermal photodesorption from the annealed particulate, $\Delta H_{\lambda a}$ is the energy required to remove carbon clusters from the annealed particulate by non-thermal photodesorption, and $P_{\lambda a}$ is the effective pressure calculated from the rate of non-thermal photodesorption from the annealed particulate. A more detailed discussion and the setting parameters that are needed for solving this equation can be found in Michelsen's work [5]. Figure 6 shows the temporal profile of sublimation.

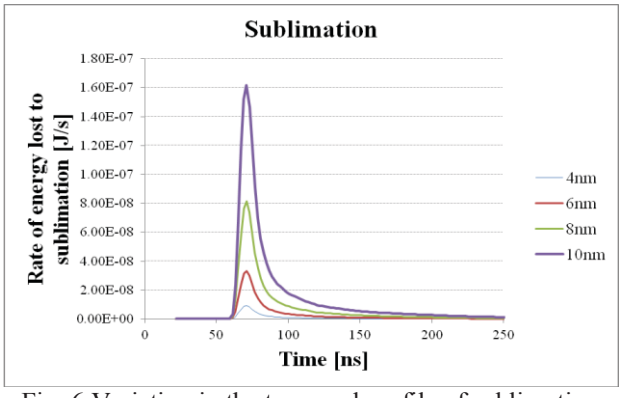

Fig. 6 Variation in the temporal profile of sublimation energy loss rate

Annealing: The annealing energy production rate was calculated as:

$$Q_{ann} = \frac{-\Delta H_{imig} k_{imig} N_d - \Delta H_{vmig} k_{vmig} N_d}{N_a} \qquad (10)$$

where ΔH_{imig} is the estimated enthalpy for interstitial migration (ΔH_{imig} = −1.9×10^4 J/mol), ΔH_{vmig} is the enthalpy for vacancy migration derived from the theoretical calculation (ΔH_{vmig} = −1.4×10^5 J/mol), N_d is the number of lattice defects in the particulate, and N_a is the Avogadro constant (6.02214×10^{23} mol^{-1}). The quantities k_{imig} and k_{vmig} are given by:

$$k_{imig,vmig} = A_{imig,vmig} \exp\left(\frac{-E_{imig,vmig}}{RT}\right) \qquad (11)$$

where A_{imig} and A_{vmig} are factors used to calculate the rate constant for interstitial migration and vacancy migration ($A_{imig} = 1\times10^{8}$ s^{-1}, $A_{vmig} = 1.5\times10^{17}$ s^{-1}); E_{imig} is the activation energy for the annealing rate associated with the di-interstitial migration ($E_{imig} = 8.3\times10^{4}$ J/mol); and E_{vmig} is the activation energy for the annealing rate from vacancy migration ($E_{vmig} = 6.7\times10^{5}$ J/mol). The quantity R is the universal gas constant (8.3145 J/mol·K). Figure 7 shows the temporal profile of annealing.

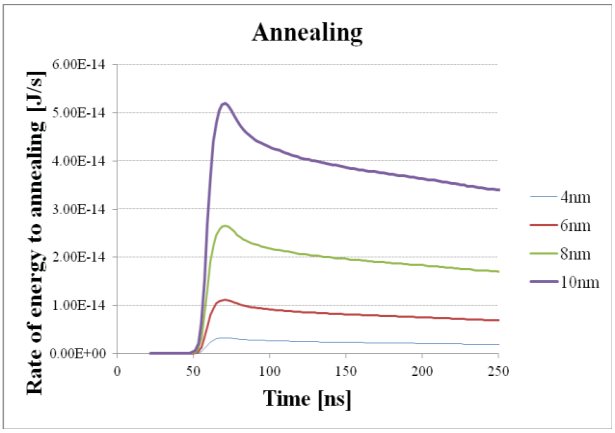

Fig. 7 Variation in the temporal profile of the annealing energy rate

Oxidation: The rate of oxidation was calculated as:

$$Q_{ox} = \left(-\Delta H_{ox} - 2\alpha_T C_P^{co} T\right)\frac{\pi D^2 k_{ox}}{N_a} \qquad (12)$$

where ΔH_{ox} is the enthalpy of reaction ($\Delta H_{ox} = -2.215\times10^{5}$ J/mol) and C_P^{CO} is the molar heat capacity of CO, given by the Fried and Howard equation:

$$C_P^{co} = \left(\frac{R}{a_4}\right)\left\{a_1\left(\frac{\theta_1}{T}\right)^2 \exp\left(\frac{\theta_1}{T}\right)\left[\exp\left(\frac{\theta_1}{T}\right)-1\right]^{-2}\right\} + \left(\frac{R}{a_4}\right)\left\{+a_2\left(\frac{\theta_2}{T}\right)^2 \exp\left(\frac{\theta_2}{T}\right)\left[\exp\left(\frac{\theta_2}{T}\right)-1\right]^{-2} + a_3 T\right\} \qquad (13)$$

The parameters are $a_4 = 1$, $a_1 = 3.494$, $\theta_1 = 1$, $a_2 = 0.98449$, $\theta_2 = 3085.1$, $a_3 = 2.6164\times10^{-5}$. In Eq. (12), k_{ox} is given by:

$$k_{ox} = 12P_{O_2}\left[\frac{k_a\chi_A}{1+k_Z P_{O_2}} + k_b\left(1-\chi_A\right)\right]\left(1-X_{ann}\right) + \frac{2.8Z_{ox}}{\sqrt{T_0}}\exp\left(\frac{-1.4\times10^{5}}{RT}\right)X_{ann} \qquad (14)$$

where P_{O2} = 1 atm, $k_a = 5.0\times10^{23}\exp(-1.255\times10^{5}/RT)$, $k_b = 5.0\times10^{21}\exp(-6.352\times10^{4}/RT)$, $\chi_A = 1/(1+k_T/k_bP_{O2})$, $k_T = 3.79\times10^{27}\exp(-4.06\times10^{5}/RT)$, and $k_Z = 21.3\exp(1.713\times10^{4}/RT)$. The annealed mass fraction X_{ann} is given by:

$$X_{ann} = 1 - \frac{N_d}{X_d N_p} \qquad (15)$$

where N_d is the number of lattice defects in the particulate, X_d is the initial density of defects in the soot, and N_p is the number of atoms in the particulate. In this calculation, X_{ann} was estimated to be 1.0×10^{-6} and X_d and N_d are considered to be uncertain. The collision rate Z_{ox} of ambient O_2 with the particulate surface is given by:

$$Z_{ox} = \frac{P_0}{k_p T_0}\sqrt{\frac{R_m T_0}{2\pi W_a}} \qquad (16)$$

This rate was derived to be 3.03×10^{22} s^{-1}·cm^{-2}. The ambient pressure is P_0; W_a is the average molecular weight (in this equation, $P_0 = 0.209$ atm, $W_a = 31.99$ g/mol); k_p is the Boltzmann constant in effective pressure units (1.3626×10^{-22} atm cm^3/K); and R_m is the universal gas constant in effective mass units (8.3145×10^{7} g cm^2/mol·K·s^2). Figure 8 shows the temporal profile of the oxidation.

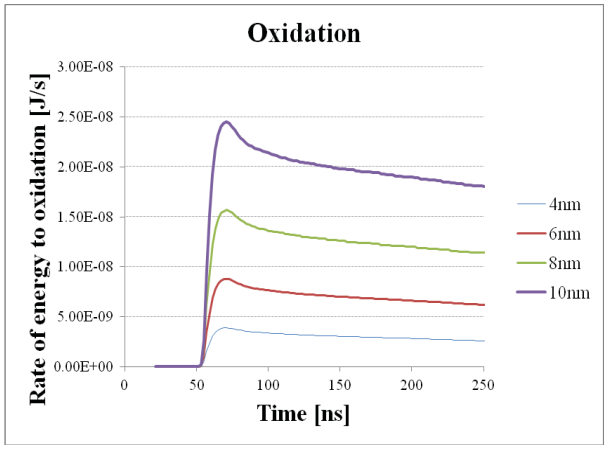

Fig. 8 Variation in the temporal profile of the oxidation energy rate

4. RESULTS

Size measurement using LII technique:

Figure 9 shows the experimental data of the time-resolved LII signals obtained from primary soot in a candle observed at a wavelength of 400 nm; it also shows the results of calculation for four different primary particulate diameters. The experimental data is indicated by asterisks. The experimental data have been normalized to the maximal signal. The results of the simulations have also been normalized to the maximal signal for each case, and were then scaled for comparison with the experimental data. When comparing the calculated profiles to the experimental data, it is seen that the temporal profile is in good agreement

with the estimations for a primary particulate diameter of 6 nm.

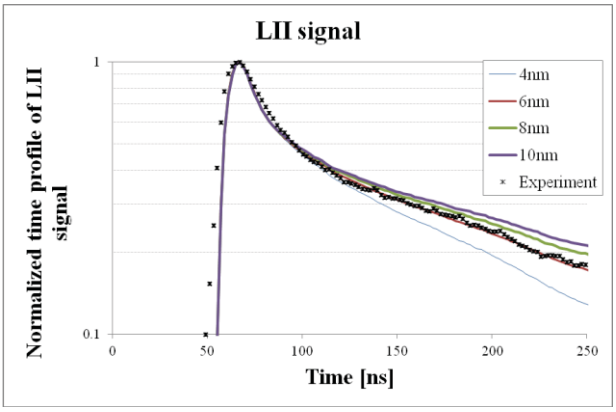

Fig. 9 Comparison of the experimental profile obtained from primary candle soot at a wavelength of 400 nm, with the normalized LII calculated profiles

Elemental analysis using LIBS technique:

Figure 10 shows carbon atomic signals obtained using the LIBS. The LIBS signals were obtained from the experimental data for a candle flame. The wavelength at 247.856 nm was determined for detecting carbon (C).

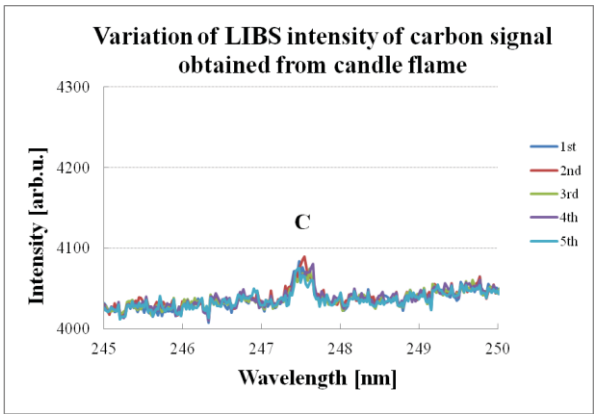

Fig. 10 Carbon atomic signals that were obtained using five successful LIBS measurements in candle flame

A different elemental analysis for SPMs using LIBS:

1. Diesel particulate matter

Figure 11 shows a SEM image of diesel particulate matter deposited on a trap filter. Particulates of various sizes, ranging from a few hundred nanometres to 20 µm, were deposited on the filter. The trap filter (TX40HI-20-WW) was used to test the exhaust emissions from a diesel engine. Figure 12 shows the atomic signals corresponding to the diesel particulate, as obtained from LIBS measurements. Peaks due to carbon (C) and boron (B) were observed in these wavelength ranges.

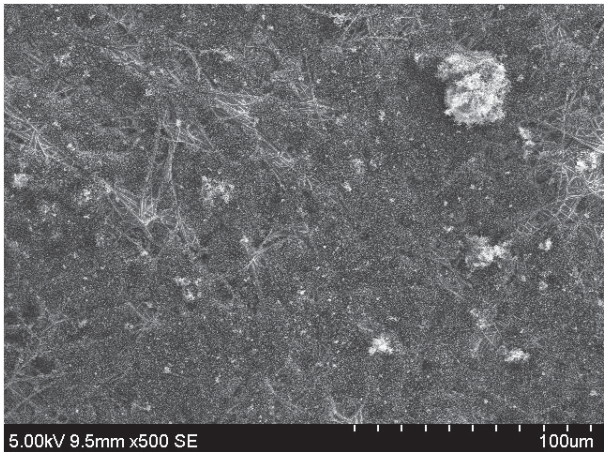

Fig. 11 SEM image of diesel particulate matter deposited on a trap filter

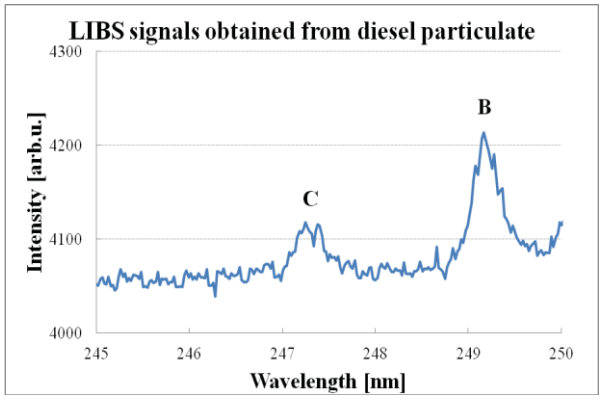

Fig. 12 Atomic signals obtained from the LIBS measurements on diesel particulates

2. Metal particulates

Figure 13 shows a SEM image of metal particulates deposited on a porous silicon filter. Particulates with sizes of 2.5 µm and less than 2.5 µm are shown in the image. The metal particulates are speculated to come from the motor brushes or to be generated during the sputtering or reflow processes during the fabrication.

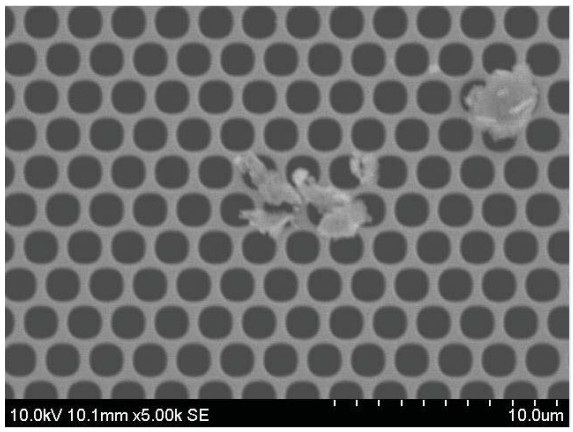

Fig. 13 A SEM image of metal particulates deposited on a porous silicon filter

Figure 14 shows the atomic signals corresponding to the copper (Cu) particulates, as obtained from LIBS measurements. From the results obtained for the nano-sized Cu sample, the wavelengths of 324.754 nm and 327.396 nm were used to detect the Cu metal particulates. Peaks due to Cu were observed in these wavelength ranges.

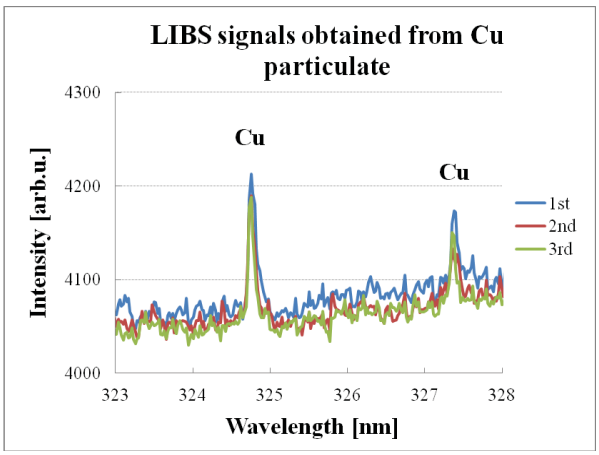

Fig. 14 Atomic signals obtained from the LIBS measurements on copper particulates

5. CONCLUSIONS

We proposed a contactless elemental and size measurement system for fine particulates. The system uses laser-induced breakdown spectroscopy and laser-induced incandescence temporal analytical techniques. When LIBS was used for measurements, the proposed system provided rapid quantitative information for the components of every kind of particulate elements. Particulate size measurement was accomplished with the help of the LII technique. In the proposed system, one can switch from LIBS to LII by merely controlling the power density of the light source that operates the measurement, without any processing of the measured objects. In the experiment on LII for primary particulates in a candle frame, the temporal profile was found to be in good agreement with the estimated primary particulate diameter of 6 nm. The particulate size obtained in this experiment was smaller than the values obtained in previous works for carbonaceous soot [6–12]. This fact indicates that LII technique allows detecting soot growing process from the early steps in the flame. The elemental spectra due to carbon, boron, and copper were observed in the LIBS experimental results that were obtained from each type of the particulates. This system allows facilitating the *in-situ* measurement system of suspended particulate matter in the air, monitoring system for oxygen supply during combustion process and detection system of the origin of metal particulates in a clean room.

6. REFERENCES

[1] Brown J.H., Cook K.M., Ney F.G., and Hatch T., "Influence of Particle Size upon the Retention of Particulate Matter in the Human Lung", American Journal of Public Health Nations Health, pp. 450-458, April (1950)

[2] Kodavanti U.P., Schladweiler M.C., Ledbetter A.D., Watkinson W.P., Campen M. J., Winsett D.W., Richards J.R., Crissman K.M., Hatch G.E., and Costa D.L., "The Spontaneously Hypertensive Rat as a Model of Human Cardiovascular Disease: Evidence of Exacerbated Cardiopulmonary Injury and Oxidative Stress from Inhaled Emission Particulate Matter", Toxicology and Applied Pharmacology, Vol. 164, No. 3, pp. 250-263, May 1 (2000)

[3] Squadrito G.L., Rafael C., Dellinger B., and Pryor W.A., "Quinoid redox cycling as a mechanism for sustained free radical generation by inhaled airborne particulate matter", Free Radical Biology and Medicine, Vol. 31, No. 9, pp. 1132-1138, November 1 (2001)

[4] Carll A.P., Haykal-Coates N., Winsett D.W., Rowan III W.H., Hazari M.S., Ledbetter A.D., Nyska A., Cascio W.E., Watkinson W.P., Costa D.L., and Farraj A.K., "Particulate matter inhalation exacerbates cardiopulmonary injury in a rat model of isoproterenol-induced cardiomyopathy", Inhalation Toxicology, pp. 1-14, early online posted February 02 (2010)

[5] Michelsen H.A., "Understanding and Predicting the Temporal Response of Laser-induced Incandescence from Carbonaceous Particles", Journal of Chemical Physics, Vol. 118, pp. 7012-7045 (2003)

[6] Megridis C.M. and Dobbins R.A., "Soot aerosol dynamics in a laminar ethylene diffusion flame", Symposium (International) on Combustion, Vol. 22, Issue 1, pp. 353-362 (1989)

[7] Köylü Ü.Ö. and Faeth G.M., "Structure of overfire soot in buoyant turbulent diffusion flames at long residence times", Combustion and Flame, Vol. 89, Issue 2, pp. 140-156 (1992)

[8] Vander Wal R.L. and Choi M.Y., "Pulsed laser heating of soot: morphological changes", Carbon, Vol. 37, Issue 2, pp. 231-239 (1999)

[9] di Stasio S., "Electron microscopy evidence of aggregation under three different size scales for soot nanoparticles in flame", Carbon, Vol. 39, Issue 1, pp. 109-118 (2001)

[10] Vander Wal R.L. and Jensen K.A., "Laser-Induced Incandescence: Excitation Intensity", Applied Optics, Vol. 37, Issue 9, pp. 1607-1616 (1998)

[11] Will S., Schraml S., Bader K., and Leipertz A., "Performance characteristics of soot primary particle size measurements by time-resolved laser-induced incandescence", Applied Optics, Vol. 37 Issue 24, pp.5647-5658 (1998)

[12] Schraml S., Dankers S., Bader K., Will S., and Leipertz A., "Soot Temperature Measurements and Implications for Time-Resolved Laser-Induced Incandescence (TIRE-LII)" Combustion and Flame, Vol. 120, Issue 4, pp. 439-450 (2000)